Direct numerical simulations of transitional pulsatile flow through a constriction

N. BERATLIS, E. BALARAS AND K. KIGER

Department of Mechanical Engineering, University of Maryland, College Park, MD, USA

A combined experimental and numerical study of transitional pulsatile flow through a planar constriction is presented. The parametric space that we adopt is similar to the one reported in a variety of past experiments relevant to the flow through stenosed arteries. In general, the flow just downstream of the constriction is dominated by the dynamics of the accelerating/decelerating jet that forms during each pulsatile cycle. We found a switch in the shedding frequency and roll-up dynamics, just after the flow rate approaches its maximum value in the cycle. The flow in the reattached area further downstream is also affected by the jet dynamics. A 'synthetic' turbulent-like wall-layer develops, and is constantly supported by streamwise vortices that originate from the spanwise instabilities of the large coherent structures generated by the jet. The relation of these structures to the phase-averaged turbulent statistics and the turbulent kinetic energy budgets is discussed.

1. Introduction

Wall-bounded pulsatile and oscillating flows are frequently encountered in many fields ranging from oceanography to biomedical sciences. To facilitate the analysis of such flows, the most commonly studied cases involve the flow through a channel or a pipe upon which a time-dependent pressure gradient is applied in a periodic fashion (i.e. Stettler & Hussain 1986; Scotti & Piomelli 2001a). However, the complexity of pulsatile pipe and channel flows is further increased when an immersed object or a constriction in the geometry is imposed. Such configurations are relevant to many biological flows. A characteristic example is the circulation of blood inside diseased arteries with various degrees of atherosclerosis. In such a case, the deposition of plaque on the walls reduces the vessel diameter and during advanced stages of the disease the blood vessels become considerably narrower, creating a constriction (or stenosis) that significantly alters the local blood flow dynamics. Flows which were initially laminar can locally transition to a disturbed or quasi-turbulent state, depending on the geometry, forcing conditions and fluid properties. From a biological aspect, the changes that take place in the flow have a profound effect on the structure and function of the arterial wall (Davies *et al.* 1986) and the development of the disease (Ku 1997; Berger & Jou 2000). Given the medical importance of this problem, as well as the rich underlying physics of the flow, a great deal of work has been done within the relatively narrow parametric space relevant to the pathology of atherosclerosis. The current work presents a combined experimental and numerical examination of an idealized flow specifically targeted in the same regime. This work is intended to build upon the existing literature as a vehicle for understanding the detailed flow

physics of transition to turbulence downstream of the obstruction that is common to flows within this range.

Early work on analysing the flow disorder in pulsatile stenotic flows focused on *in vivo* measurements of blood velocity. Khalifa & Giddens (1978), for example, studied the velocity signal in the descending thoracic aorta of dogs with a controlled degree of stenosis. They considered Reynolds numbers in the range of $1000 < Re_m < 1200$ (Re_m is based on the average bulk velocity during the pulsatile cycle and the unoccluded diameter upstream of the stenosis), and varied the reduction in area caused by the stenosis up to a maximum of 88 %. They observed that even mild occlusions yielded flow disorder immediately downstream of the stenosis. The instabilities commenced around the peak systolic velocity, and as the degree of occlusion increased, so did the duration of flow disorder. Energy frequency spectra were calculated for four short intervals during the cycle. It was found that as the degree of stenosis increased, the spectra during the deceleration phase exhibited a higher and broader energy content. Another example of *in vivo* measurements of intravascular pressure fluctuations and blood flow velocity in a surgically induced stenosis at the pulmonary artery of calves has been reported by Lu, Gross & Hwang (1980). Their work was motivated by the fact that the turbulence in the post-stenotic region generates acoustic sounds and murmurs, with a postulate that proper interpretation of these murmurs can prove a diagnostic tool of cardiovascular diseases. They also divided the pulsatile cycle into four time intervals and computed pressure and velocity spectra for each interval. They found that the energy spectra exhibited a $-5/3$ slope during early to late systole up to approximately 100 Hz and then suddenly changed to a $-10/3$ slope. They attributed this change of slope (or break) to transfer of turbulent kinetic energy into acoustic fluctuations. Support for this conjecture was drawn from the fact that the sound (or pressure) spectra exhibited a rise in intensity at a frequency immediately following the break in frequency of the energy spectra. In addition, the break frequency in the pressure spectra was not dependent upon the percentage of stenosis or the jet peak velocity.

Although *in vivo* studies have highlighted the turbulent characteristics of the post-stenotic region, they failed to elucidate the mechanisms that caused the flow to transition. This was due to limited measurement capabilities and inherent difficulties in conducting animal experiments under closely controlled conditions. Significant progress, however, in understanding the fluid dynamics of post-stenotic flows has been made utilizing idealized *in vitro* studies. A variety of experiments by Giddens and co-workers (i.e. Cassanova & Giddens 1978; Khalifa & Giddens 1981; Ahmed & Giddens 1984; Lieber & Giddens 1990; Ojha *et al.* 1984; and Siouffi, Deplano & Pelissier 1998) among others, have been reported over the past decades. In most cases, the experimental conditions were not representative of a specific segment of the human anatomy but, rather, designed to isolate the main phenomena that dominate the dynamics of the flow. In particular, the arteries were assumed to be rigid, straight pipes with sharp or contoured constrictions, and various degrees of stenosis. The flow conditions were selected to be within the same range as in previous *in vivo* studies mentioned above, and in most cases the flow upstream of the constriction was laminar throughout the pulsatile cycle. In the poststenotic region, however, a highly complex, multi-step process of transition to turbulence was observed. Initial disturbances appear during the higher velocity portion of the pulse, preceded by a large, low-frequency fluctuation. Based on flow visualizations and velocity measurements, Cassanova & Giddens (1978) and Ahmed & Giddens (1984) speculated that the latter was caused by a 'start-up' vortex forming downstream of the constriction, and swirling into the region

near the wall. Following this structure, a quasi-periodic array of vortices is generated, probably as a result of a Kelvin–Helmholtz-type instability in the shear layer. Lieber & Giddens (1990) found that the amplitude and shedding frequency of the vortices can change by a factor of two during the pulsatile cycle. The breakdown of these structures and their interaction with the wall, primarily during the deceleration phase leads to very high turbulent intensities in the region just after the mean reattachment point.

While such experiments have successfully demonstrated the existence of a shear layer instability and vortex shedding, they did not provide adequate resolution to quantify the spatio-temporal evolution of the turbulent structures. Thus, in recent years, numerical tools have also been utilized to analyse the poststenotic flow field. A significant amount of computational work has concentrated on solving the Reynolds-averaged Navier–Stokes (RANS) equations coupled with a turbulence model to predict the phase-averaged flow field (Varghese & Frankel 2003; Ryval, Straatman & Steinman 2004; Stroud, Berger & Saloner 2002). Although such simulations have a relatively low computational cost and allow long integration times owing to the relaxed spatial and temporal resolution, they suffer from inherent difficulties associated with turbulence modelling. One difficulty comes from the fact that most of these models were developed for equilibrium turbulent wall-bounded flows, and so they are not well-suited for flows with separation and reattachment zones or transitional flow patterns such as the ones shown in the experiments. Scotti & Piomelli (2001b) tested various turbulence models for the unsteady RANS equations using a direct numerical simulation (DNS) database of turbulent pulsatile channel flow. Their results showed that the Reynolds stresses, turbulent kinetic energy, and dissipation were significantly overestimated. The development of suitable closure models, if advisable at all, would be contingent on first having a detailed knowledge of how turbulent kinetic energy is produced, dissipated and transported in the poststenotic region.

In order to circumvent the uncertainties posed by such modelling strategies, one can approach the problem through the use of increased resolution (and expense) by performing DNS and/or large-eddy simulations (LES) of the flow. Mittal, Simmons & Udakumar (2001) reported DNS and LES of pulsatile flow in a planar model of an asymmetric stenosis with 50 % occlusion and a mean Reynolds numbers in the range of $375 < Re_m < 1000$. The imposed asymmetry forced the shear layer that separates at the lip of the stenosis to tilt towards the opposite side of the channel. For all cases with $Re_m > 500$ the separated shear layer rolled up into a series of vortices reminiscent of a Kelvin–Helmholtz-type instability. The effect of these transitional patterns on the wall region after the reattachment point were assessed by spectral analysis. The frequency spectra of the streamwise velocity in that region exhibited a break from $-5/3$ to a -7 slope at roughly the frequency corresponding to the frequency of vortex shedding. This suggested the existence of possible turbulent-like flow with a well-defined inertial subrange. More recently, Sherwin & Blackburn (2005) performed a numerical study of both steady and pulsatile axisymmetric stenotic flows with a smooth 75 % constriction at mean Reynolds numbers in the range of $250 < Re_m < 550$. Floquet stability analysis revealed that all the leading unstable modes arise through a period-doubling bifurcation whose main characteristic was to alternately tilt the vortex rings forward and backwards. Subsequent flow visualizations from DNS confirmed the existence of such a mode and showed that the breakdown of the vortex rings leads to the formation of streamwise-oriented vortical structures. In addition to these phenomena, a shear layer oscillation was observed only when high-frequency and low-amplitude perturbations were added at the inflow.

From the brief literature survey above, it is evident that significant progress has been made in understanding the basic mechanisms that lead to transitional flow patterns in stenotic pulsatile flows. Central to this process appears to be the formation of large vortical structures that undergo complex three-dimensional instabilities transforming primarily spanwise into streamwise vorticity. There are, however, several outstanding questions: How do these vortices interact with the wall and break down, and what is the effect of the breakdown process on the reattached layer? Are the structures that emerge in the reattached layer similar to the ones observed in turbulent wall-bounded flows? How is turbulent kinetic energy produced, transported and dissipated in the post-stenotic region? To clarify these issues, we have performed closely coordinated DNS and experiments. The experiments are used primarily to establish the accuracy of the DNS, which will to be the main tool in our analysis. In the following section, a brief description of the experimental and numerical methodologies will be given. Then, a detailed comparison between the DNS and the experiments will be presented. In the results section we will focus on the spatial–temporal evolution of the structures responsible for the generation of turbulence and their effect on the phase-averaged statistics and turbulent kinetic energy budgets. Finally, a brief summary and conclusions will be given.

2. Problem formulation and parametric space

In the present study we will limit the discussion of the results to a flow through a planar channel with a 50 % smooth symmetric constriction. This idealized planar configuration served as the starting point of a series of computations of increasing complexity aimed at isolating the important flow phenomena that dominate the dynamics of the actual, more complex, problem. Compared to an equivalent axisymmetric configuration, where usually the mean flow is three-dimensional and unsteady, the present geometry allows spatial averaging along the homogeneous direction. This increases substantially the statistical sample, making feasible the convergence of higher-order statistics. The parametric space was chosen to be within the physiologic regime considered in prior *in vitro* experiments available in the literature for the purpose of investigating the robustness and repeatability of the observed flow phenomena. The above parametric space obviously does not account for all factors that can influence the dynamics of such flows (i.e. curvature, wall roughness, non-sinusoidal flow rate, wall compliance, rheological effects, etc.). As we will discuss in the result section, however, the flow physics reproduced in this simplified configuration are qualitatively similar to the ones reported in a variety of *in vivo* and *in vitro* experiments with various degrees of complexity, thus allowing a more detailed understanding of the relevant first-order fluid dynamic effects associated with post-stenotic transition.

As shown in figure 1(*a*), we consider a channel with a semicircular constriction on both walls. The stenosis is uniform across the span and symmetric about the centre of the channel. The coordinates of the stenosis with respect to the centreline are given by

$$\left(\frac{z \pm z_0}{h} \right)^2 + \left(\frac{x}{h} \right)^2 = R, \tag{2.1}$$

where h denotes half the channel height, x and z are the streamwise and wall-normal coordinates respectively, z_0 is the centre offset of the cylindrical obstruction, and R is the radius of the cylinder. In all the cases investigated in the current work, values of $z_0/h = 1.5$ and $R/h = 1$ have been used, resulting in a 50 % occlusion and a stenosis length $\lambda = \sqrt{3}h$.
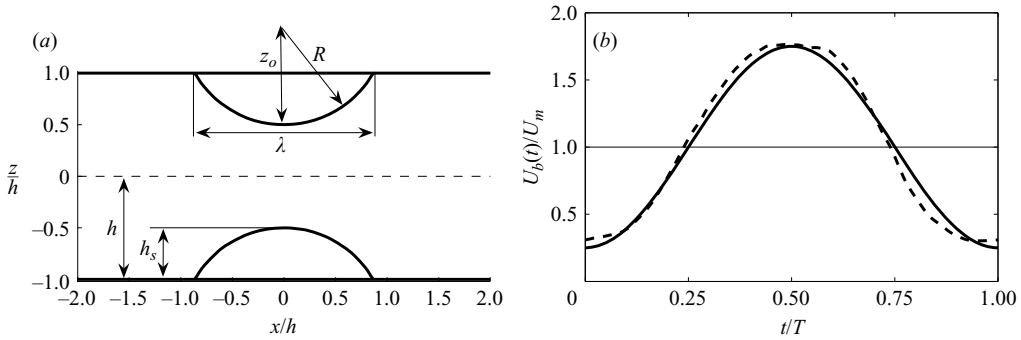
FIGURE 1. (*a*) Geometrical parameters that define the stenosis.
(*b*) Waveform of $U_b(t)$: – – – case 1; —— case 2.

Case	Re_m	α	U_{red}	K	Domain size	Grid resolution	Inlet conditions
1	600	8.4	26.5	1.75	$60 \times 6 \times 2$	$598 \times 64 \times 102$	$\tilde{u}_{experiment} +$ noise
2	600	16.8	6.6	1.75	$60 \times 6 \times 2$	$598 \times 64 \times 102$	$\tilde{u}_{analytical} +$ noise
3	600	8.4	26.5	1.75	$60 \times 6 \times 2$	$598 \times 64 \times 102$	$\tilde{u}_{analytical} +$ noise
4	600	4.2	106.2	1.75	$70 \times 6 \times 2$	$832 \times 64 \times 102$	$\tilde{u}_{analytical} +$ noise
5	1200	8.3	53.1	1.75	$60 \times 6 \times 2$	$598 \times 128 \times 102$	$\tilde{u}_{analytical} +$ noise

TABLE 1. Summary of cases studied.

The flow conditions upstream of the constriction are defined using the following parameters: the mean Reynolds number $Re_m = U_m h/\nu$ (U_m is the time-average bulk velocity and ν the kinematic viscosity); the Womersley number, $\alpha = h(2\pi/T\nu)^{0.5}$ (T is the period of the oscillation); and the non-dimensional amplitude of the oscillations, K, defined as the ratio of the maximum bulk velocity, U_{max} to U_m. The reduced velocity, $U_{red} = U_m T/2h$, is also a useful parameter and can be interpreted as the ratio of the mean convective length to the channel height. Note that U_{red} is not an independent parameter and is related to the Reynolds number and α according to the relation $U_{red} = \pi Re/\alpha^2$. Table 1 summarizes the range of these parameters in our simulations. We considered three different forcing frequencies ($4.2 < \alpha < 16.8$) and two Reynolds numbers ($Re_m = 600$ and 1200) while keeping the amplitude of the oscillations constant. Thus the reduced velocity also varies from $U_{red} = 6.6$ to 106.2. In all cases except case 1, the temporal characteristics of the bulk velocity consist of a mean plus a single harmonic. For case 1, however, the flow rate was set to match that of the experiment, which deviates from a single-frequency sinusoid due to limitations in fine-tuning the spool valve in the experimental apparatus. To quantify the effect of this small deviation on the results, we compared first- and second-order velocity statistics between cases 1 and 3. The results for these two cases were very close and therefore we consider them as equivalent.

3. Methodologies

3.1. *Experimental facility*

The experimental measurements were completed in a closed-return pulsatile facility as illustrated in figure 2. The test section was composed of a planar acrylic channel with interior dimensions of $1830 \times 150 \times 12.5$ mm, in the streamwise, spanwise and
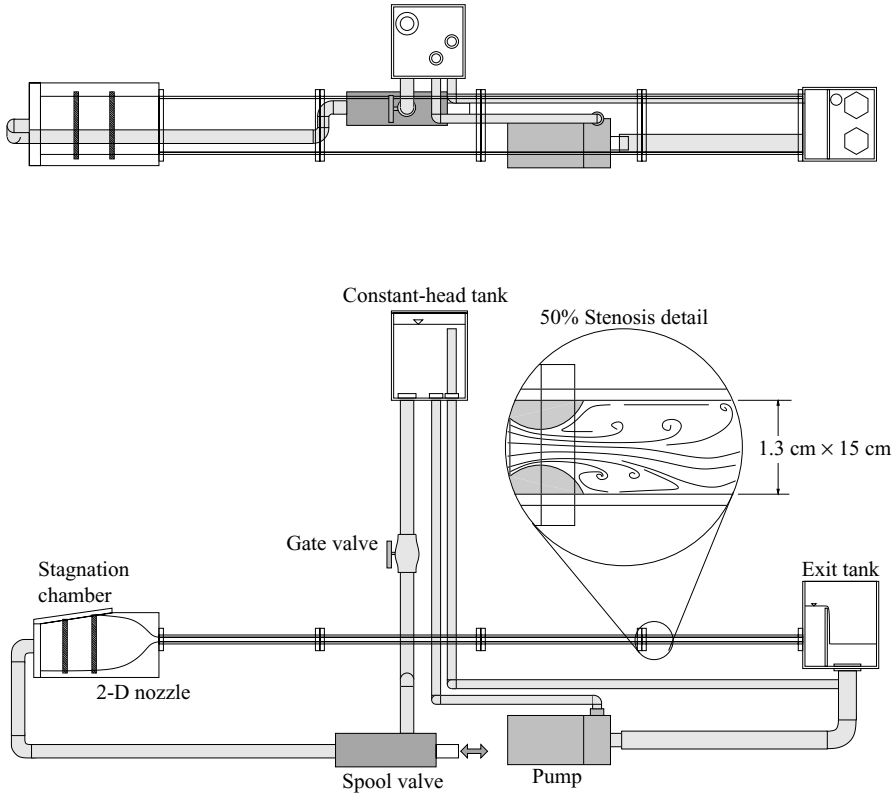
FIGURE 2. Top and side views of a schematic of the experimental setup.

wall-normal directions, respectively ($292h \times 24h \times 2h$, in terms of channel half-height, h). A symmetric stenosis was created in the shape of the two cylindrical segments shown in figure 1(*a*). The stenosis was placed $220h$ from the channel entrance to ensure fully developed flow upstream of the constriction, while still providing approximately $70h$ in which to make measurements within the post-stenotic region. Upstream of the test section entrance, a two-dimensional contraction with an area ratio of 10 : 1 provided the transition between the stagnation chamber and test section. Within the stagnation chamber, a series of two open-cell foam filters and stainless steel screens were used to provide a low-turbulence uniform flow to the nozzle contraction. The flow through the test section was supplied by a constant-head tank elevated approximately 1 m above the exit tank free surface, which was maintained at this level by an overflow return and a vibration-isolated centrifugal pump. The mean flow was controlled by an adjustable gate valve, while the oscillatory component was generated through the use of a custom-built spool valve. The spool valve orifice was designed to provide a linear variation in flow rate with respect to the stroke position of the spool, allowing the use of a crank-arm and slider mechanism to produce a nominally sinusoidal oscillation of the flow. In practice, however, the valve characteristics were slightly nonlinear, and finite tolerances in the linkage contributed to a small, but noticeable, dwell in the flow-rate profiles as a function of time (see figure 1*b*).

Detailed measurements of the flow characteristics were made using single-component laser Doppler velocimetry (LDV). The measurement system consisted of a Dantec instrument (BSA P50 processor, FiberFlow 60X63 transceiver with beam

expander) and computer-controlled traverse system. The flow was seeded with hollow borosilicate glass spheres (Sphericel 110P8, by Potters Industries) nominally 10 μm in diameter with an effective specific gravity of 1.1. The particles were added in sufficient concentration to allow a mean sampling rate of 150 Hz. The mean bulk velocity was set to $\overline{U}_m = 0.082\,\mathrm{m\,s^{-1}}$, with an oscillatory amplitude of $\Delta U_m = 0.06\,\mathrm{m\,s^{-1}}$ and a period of $T = 4\,\mathrm{s}$. Water was used as the working fluid, and after several hours of warm-up operation, the temperature of the liquid stabilized to 25 °C, giving a kinematic viscosity, $\nu = 9 \times 10^{-7}\,\mathrm{m^2\,s^{-1}}$. With the above dimensional values, the corresponding Reynolds and Womersley numbers are $Re_m = 570$ and $\alpha = 8.25$, respectively. Profiles of the streamwise velocity were then recorded at six different streamwise stations ($x/2h = -10, +2, +4, +6, +10$ and $+20$) with 0.5 mm intervals in the wall-normal direction (25 positions in each profile). Each position was sampled for a duration of 100 cycles. The arrival time of the samples was marked relative to the opening stroke of the spool valve, allowing the data to be ensemble averaged with respect to the phase of the bulk flow oscillation. In generating the phase-averaged data, each cycle was divided into 90 equally sized bins (see the Appendix for details on the data reduction). The number of samples at each position varied depending on the velocity at that particular position in space and time, but the typical value was on the order of 600 samples per bin.

3.2. *Numerical techniques and boundary conditions*

In all the simulations reported in this study, the fluid is assumed to be Newtonian and the flow incompressible. A fractional step method is used for the time advancement, and all spatial derivatives are approximated with second-order central differences on a staggered grid. A Cartesian grid is used throughout the domain. The stenosis, which is not aligned with the grid lines, is introduced using an embedded-boundary formulation. Details on the methodology and an extensive validation in laminar and turbulent flows can be found in Balaras (2004). No-slip conditions are enforced on all solid boundaries, and periodic boundary conditions are used in the homogeneous, spanwise direction. A convective boundary condition that allows disturbances to propagate out of the domain without influencing the rest of the computational box is used at the outflow plane (see Orlansky 1974).

Given the sensitivity of transitional flows to the disturbance environment, detailed measurements were taken upstream of the stenosis to guide the specification of the inflow boundary conditions in the simulations. These measurements showed that during part of the pulsatile cycle the flow upstream of the stenosis undergoes a transition from a laminar to a 'disturbed-laminar' state as a result of an instability associated with the inflection points in the velocity profiles. To reproduce this environment the velocity field specified at the inflow plane consisted of two parts: (i) a time-varying mean component that is obtained either from interpolation of the experimental velocity profiles in case 1, or from the analytical solution (see Panton 1996, pp. 272–277) in all other cases; (ii) a perturbation component, that is introduced to trigger instabilities when inflection points are present in the laminar profiles. To prevent the random component from decaying a few grid cells downstream from the inflow plane, we used synthetic isotropic turbulence based on the formulation developed by Rogallo (1981). This procedure produces fluctuations that are isotropic, satisfy the continuity equation and have the von Kármán energy spectrum. The fluctuations were scaled to have the magnitude of the background noise in the experiments, and were smoothly reduced to zero near the walls using a hyperbolic tangent function. Details on the specification of the inflow boundary conditions together with a comprehensive study on the effects

of the size of the computational box and grid resolution, can be found in Beratlis *et al.* (2005). That study was also used as a guide to select the grid resolution and domain size for the computations reported in the present work. A summary of the corresponding parameters is given in table 1.

In both experiments and simulations, two different types of averaging operators were utilized for the data reduction. A quantity, $f(x, y, z, t)$, can be averaged in time, as well as in space along the homogeneous direction (y lines) as follows:

$$\overline{f}(x, z) = \frac{1}{T_{tot} L_y} \int_0^{T_{tot}} \int_0^{L_y} f(x, y, z, t) \, dy \, dt \qquad (3.1)$$

where $T_{tot} = NT$ is the total time of integration, and N is the number of periods, T, over which the equations are integrated. L_y is the spanwise length of the computational domain. A phase-averaging operator was also constructed, which is very effective in extracting the response of the flow to the pulsatile frequency, as follows:

$$\widetilde{f}(x, y, z, t) = \frac{1}{N} \frac{1}{L_y} \sum_{n=1}^{N} \int_0^{L_y} f(x, y, z, t + nT) \, dy. \qquad (3.2)$$

The fluctuations with respect to the long-time and phase averages will be denoted by a prime and double prime respectively:

$$f'(\boldsymbol{x}, t) = f(\boldsymbol{x}, t) - \overline{f}(x, z), \qquad f''(\boldsymbol{x}, t) = f(\boldsymbol{x}, t) - \widetilde{f}(\boldsymbol{x}, t).$$

The implementation of the phase-averaging operator given by equation (3.2) in the numerical simulations is straightforward. In the case of the experiments, however, because of the stochastic single-point nature of the experimental measurements a slightly different expression, denoted by $\langle \rangle$, was utilized. Details are given in the Appendix.

Special attention was also given to calculating the frequency power spectra of the streamwise velocity signals in the experiments and computations. Because of the unsteady quasi-periodic nature of the flow and the fact that the discrete points on the signal are not equidistant, a direct Fourier-transform of the signal or its segments is not possible. To remove spectral information associated with the quasi-periodic temporal variation of the flow, we fit a second-order polynomial in a least-squares sense to the segment of the velocity signal under consideration and subtract it from the signal. This operation results in applying a high-pass filter to the data in order to minimize the effect of the periodic mean component of the signal. Polynomials up to fourth order were also tested and the peak in the frequency spectra did not change much (variation less than 5 %). We then use a 'slotting' technique, in which the autocorrelation function together with its discrete separation distances is calculated from the signal (details on the implementation of the 'slotting' technique, which is based on the formulation developed by Mayo (1978), can be found in Poelma (2004) and Poelma, Westerweel & Ooms (2006). The separation distances are then discretized into equally spaced bins or 'slots' and the power spectra are obtained either by FFT or an autoregressive method of the autocorrelation function. The later gives better resolution when the signal is short and was particularly useful in estimating the Strouhal number for the shedding frequency of the shear layer oscillations.
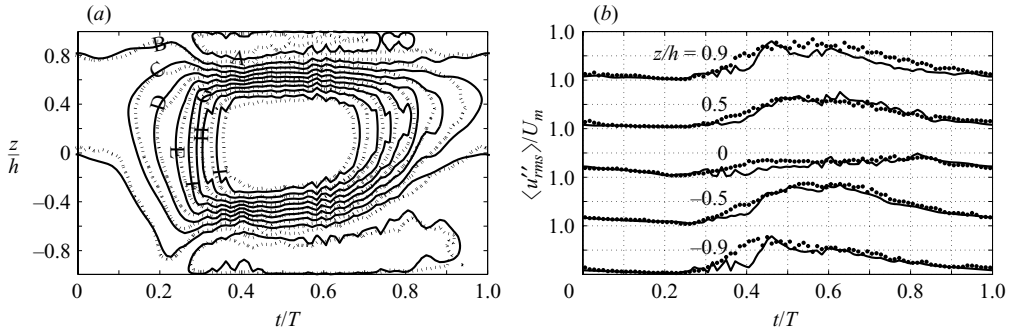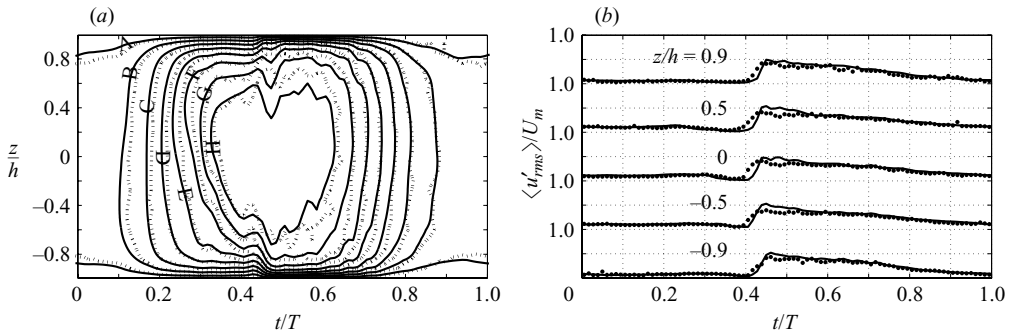
FIGURE 3. Spatio-temporal exvolution of the phase-averaged statistics of (a) $\langle U \rangle / U_m$ and (b) u''_{rms} / U_m at $x/h = 4$. ⋯⋯⋯, present experiment; ——, case 1. Index values for the contour levels in (a) are A $= -0.18$; B $= 0.38$; C $= 0.76$; D $= 1.13$; E $= 1.15$; F $= 1.89$; G $= 2.26$; H $= 2.63$; I $= 3.01$.

FIGURE 4. Spatio-temporal evolution of the phase-averaged statistics of (a) $\langle U \rangle / U_m$ and (b) u''_{rms} / U_m at $x/h = 12$. ⋯⋯⋯ present experiment; —— case 1. Index values for the contour levels in (a) are A $= 0.23$; B $= 0.46$; C $= 0.70$; D $= 0.97$; E $= 1.16$; F $= 1.40$; G $= 1.62$; H $= 1.85$.

4. Results and discussion

4.1. *Comparison between experiments and simulation*

Before analysing the DNS database that covers the parametric space given in table 1, the baseline test case (case 1) is compared to the experiment to establish the accuracy of the simulations. In this section, we will present comparisons for the phase-averaged statistics and power frequency spectra at some characteristic locations downstream of the constriction. Figures 3(a) and 4(a) show iso-contours in the z/h versus t/T space of $\langle U \rangle$ across the channel at $x/h = 4$ and $x/h = 12$ respectively. The former location is within the recirculating area just downstream of the constriction, and the latter is downstream of the mean reattachment point. Accompanying these figures are plots of the time evolution of $\langle u''_{rms} \rangle$ at locations near the wall ($x/h = \pm 0.9$), at the height of the stenosis ($x/h = \pm 0.5$) and at the centreline ($x/h = 0$).

As it can be seen in figure 3(a), a strong jet is formed near the stenosis as the flow rate increases. The jet is symmetric for most of the cycle, while towards the end of the deceleration (from now on, and unless otherwise stated, we will use 'deceleration phase' to describe the part of the pulsatile cycle where the flow rate decreases from its maximum value at $t/T \sim 0.5$ to its minimum at $t/T \sim 1.0$, and 'acceleration phase' to describe the remaining part from $t/T \sim 0$ to $t/T \sim 0.5$) it becomes asymmetric
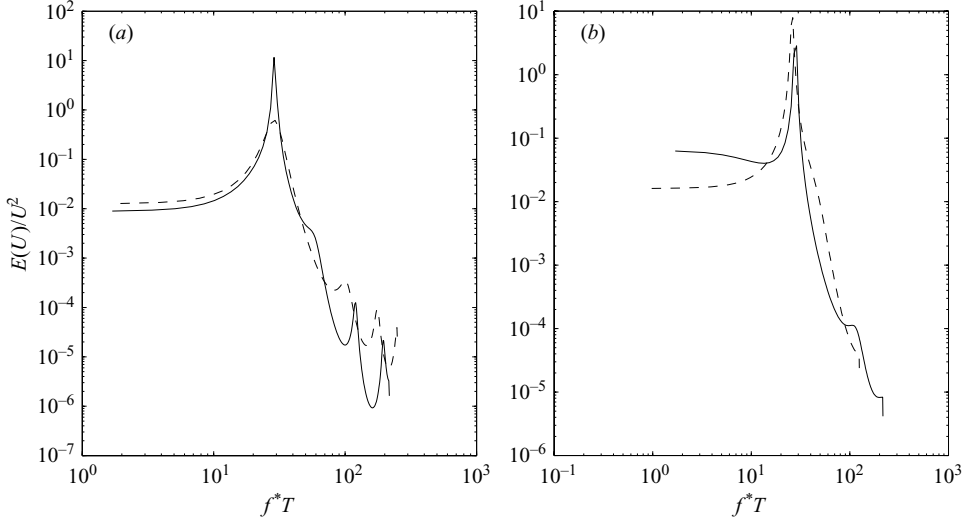
FIGURE 5. Autoregressive power spectra at $x/h = 4$ for segment of U between $t/T = 0.80$ and 0.90. ——, case 1; - - -, present experiment. (a) $z/h = -0.5$ and (b) $z/h = 0.5$. In both cases the kinetic energy in the segment has been used for normalization.

and gradually tilts towards the upper side of the channel. Near the wall, thick regions of reversed flow exist as indicated by the iso-contours of negative velocity. Qualitatively, the agreement with the experiment is excellent at this location, and the simulation captures accurately the formation and evolution of the confined jet and the recirculation bubbles throughout the cycle. From a quantitative perspective, the simulations always compare within 8 % of the experimental value, with a mean discrepancy of 5 % (based on the mean bulk velocity).

The phase-averaged, root-mean-square fluctuation of the streamwise velocity component, $\langle u''_{rms} \rangle$, as plotted in figure 3(b), highlights some important aspects of the dynamics of the shear layers at the edges of the jet. The r.m.s. levels during the early part of the acceleration are very small, indicating that any initial oscillations in the shear layer are coherent and repeatable from cycle to cycle. Later in the acceleration, however, the u''_{rms} levels increase sharply, pointing to a possible transition to a turbulent state. The $\langle u''_{rms} \rangle$ levels remain high during most of the deceleration. The agreement between the simulation and the experiments is very good (within 5 %), apart from a small interval, approximately $t/T = 0.80$–0.95, during which the latter are higher. This difference is most likely because the confined jet becomes unstable a little closer to the stenosis in the experiments, although this trend could not be confirmed with the limited number of profiles sampled in the experiment. We can verify, however, that our simulations successfully capture the dynamics of the shear layers in the experiments, by comparing the power spectrum of streamwise velocity at this downstream location. Figure 5 shows a comparison of the frequency spectra at two positions selected to be within the top and bottom shear layers during the time interval $t/T = 0.30$–0.40. The dominant peak corresponding to the vortex shedding frequency of the shear layers can be clearly observed in both cases. The Strouhal number ($N_s = 2\pi f h / \overline{U}_c$, where $\overline{U}_c$ is the time-average centreline velocity at the throat of the stenosis) at both locations is approximately 7.7, and it is the same (within 1 %) in the DNS and experiments.

The corresponding velocity statistics downstream of the mean reattachment point are also shown in figure 4. The absence of reversed flow patterns near the wall throughout the cycle indicate that the velocity profiles deviate considerably from the laminar solution. In particular, during the late acceleration and midway through the deceleration, the velocity profiles exhibit a steep velocity gradient at the wall and a relatively flat shape towards the centre of channel, indicating that significant momentum transport takes places across the channel. The apparent turbulent nature of this region of the flow will be discussed in detail in §4.3, with a focus on the turbulent kinetic energy budgets. As with the statistics at the location closer to the stenosis discussed above, the agreement with the experiment in this region is excellent.

Finally, a comparison of $\langle u''_{rms} \rangle$ at $x/h = 12$ depicted in figure 4(b) shows that the agreement with the experiment is very good at this location as well. This reinforces the conviction that the simulation captures both qualitatively and quantitatively the essential features of the flow in the post-stenotic region. Interestingly, one may note that although during most of the acceleration the $\langle u''_{rms} \rangle$ levels are low, there is a sudden spike in the streamwise turbulent intensity just before the peak flow rate. This burst in incoherent fluctuations in the wall layer lags the one observed at $x/h = 4$ by about $0.12 t/T$. If one assumes that the observed jump in $\langle u''_{rms} \rangle$ stems from an evolution of the incoherent fluctuations noted upstream, the resulting propagation velocity is calculated to be equal to the local mean velocity during that time interval ($1.2 U_m$). Therefore, this 'turbulent' front can be plausibly linked with the breakdown of the vortices originating in the mixing layer. This process will be discussed in greater detail in the following section.

4.2. *Instantaneous flow dynamics*

Having established the accuracy of the simulations in reproducing the complex transitional flow patterns in the experimental apparatus, the discussion in this section will utilize the wealth of information provided by the simulations to explore the instantaneous flow dynamics in more detail. We will start by identifying the coherent structures that dominate the dynamics of the flow and explore their spatio-temporal evolution. The effect of these structures on the phase-averaged statistics, and the way turbulent kinetic energy is produced, transported, and dissipated will be presented in the subsequent section.

As the flow rate starts to increase from its minimum value at $t/T \sim 0$, a confined jet starts to form through the constriction. To illuminate the basic flow patterns during the initial stages of the jet formation, figure 6 shows iso-contours of the instantaneous spanwise vorticity at an (x, z)-plane for case 1 from four instances during the interval $0 < t/T < 0.5$. In the proximal area downstream of the constriction, the flow remains quasi-two-dimensional during this period, indicating that these contours are a good representation of the flow throughout the spanwise direction. Superimposed on the contours are velocity streamlines highlighting the shape and evolution of the recirculating zone. Initially, the attached thin shear layers that form on the walls of the stenosis separate owing to the adverse pressure gradient induced by the expansion in the geometry, and create a closed separated area just downstream of the constriction (see figure 6a). During this early stage, the vorticity imparted into the shear layers is primarily convected downstream along the edge of the recirculation bubble. At $t/T = 0.23$ (see figure 6e), the shear layer begins to curl towards the wall, but does not immediately roll up into a vortex, as is often found in starting transients of free jets. This is most likely due to the close proximity of the solid boundaries, but may also be delayed by strong diffusion effects at these relatively low Reynolds
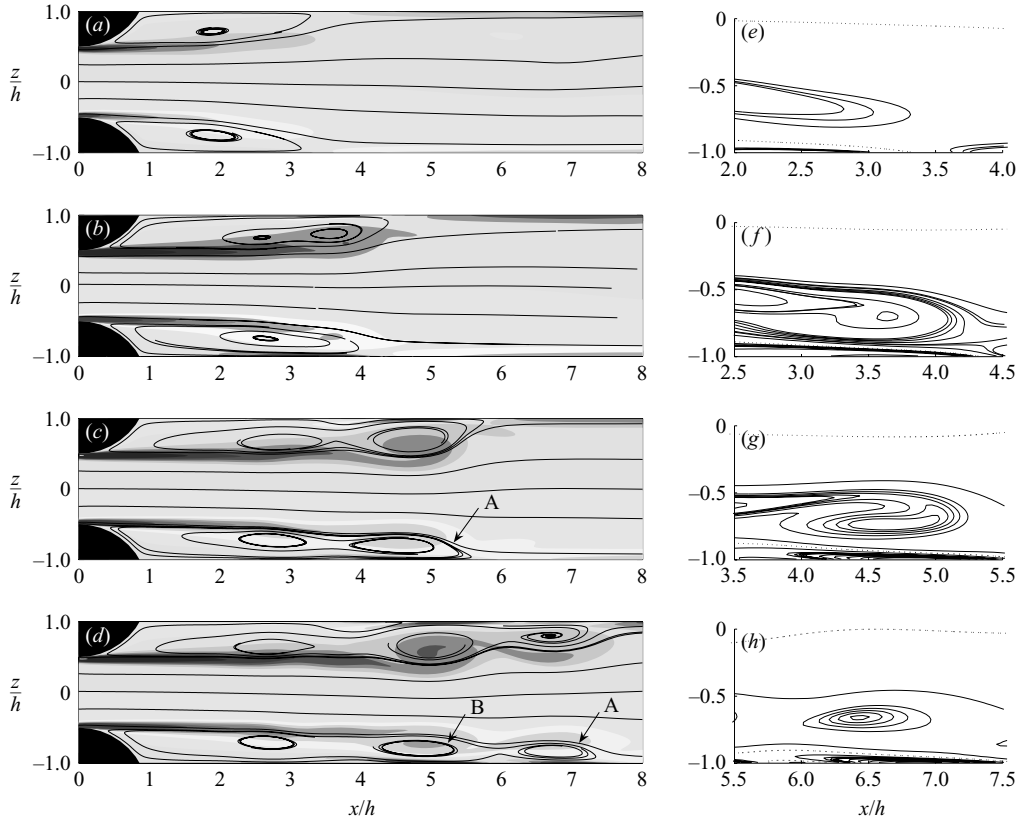
FIGURE 6. Filled iso-contours of spanwise vorticity and velocity streamlines for case 1 at four instances during the acceleration (*a–d*) and detailed iso-contour lines of spanwise vorticity following the downstream edge of the vortex sheet (*e–h*). The dotted line in (*e–h*) represents the iso-contour of zero spanwise vorticity. (*a, e*) $t/T = 0.23$, (*b, f*) $t/T = 0.28$, (*c, g*) $t/T = 0.32$, (*d, h*); $t/T = 0.36$).

numbers. Later in time though ($t/T = 0.28$), the vorticity at the tip of the shear layer eventually does initiate a roll-up into a small vortical structure, as shown in figures 6(*b*) and 6(*f*). This structure (labelled A) gradually gains strength, and at $t/T \sim 0.32$ detaches from the shear layer as indicated by the shape of the streamlines and the vorticity contours in figures 6(*c*) and 6(*g*).

As a possible explanation for the observed behaviour, one may speculate that the formation dynamics of the leading structure, A, share some of the features found in round jets accelerating in a quiescent unbounded environment (see Gharib, Rambod & Shariff 1998; Rosenfeld, Rambod & Gharib 1998). In such a case, the shear layer around the edge of the jet rolls up, forming a vortex with a circulation that continues to grow until a critical threshold is reached: at this point the vortex disconnects from the trailing jet and propagates at its own speed. This process has also been found to have a universal scaling characterized by a non-dimensional time scale of the pinch-off, referred to as the 'formation number' (Gharib *et al.* 1998). To elucidate the dynamics of the initial shear layer roll-up and robustness of the 'pinch-off' process in our simulations, we compared the results from all the different cases in table 1. The temporal and spatial localization of the initial roll-up is a complicated process probably influenced by the Reynolds number, frequency and amplitude of
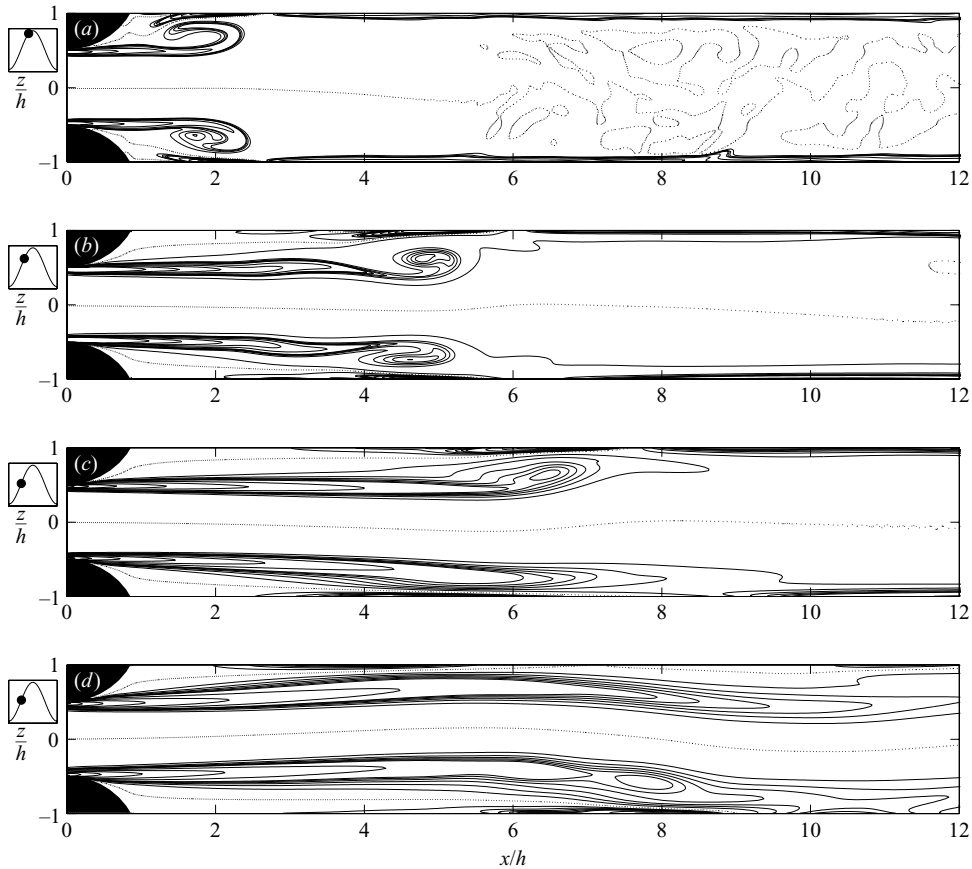
FIGURE 7. Selected iso-contours of spanwise vorticity and velocity streamlines at a characteristic instance during the initial shear layer roll-up. The dotted line represents the iso-contour of zero spanwise vorticity. (*a*) case 2, $U_{red} = 6.6$, $t/T = 0.41$; (*b*) case 3, $U_{red} = 26.5$, $t/T = 0.32$; (*c*) case 5, $U_{red} = 53.1$, $t/T = 0.26$; (*d*) case 4, $U_{red} = 106.2$, $t/T = 0.26$.

the oscillations as well as the geometry of the constriction. For our limited range of parameters, however, it is observed to vary strongly with the reduced velocity. In figure 7, selected iso-contours of the instantaneous spanwise vorticity are shown at an (x, z)-plane. As U_{red} increases (top to bottom in the figure) the jet becomes longer and the 'pinch-off' occurs farther downstream. In addition, the initial shear layer roll-up occurs earlier in time relative to the period of pulsation. Similar trends have also been observed in simulations (Rosenfeld *et al.* 1998) and experiments (Gharib *et al.* 1998) of round jets accelerating in a quiescent unbounded environment. In our case, however, we did not find the same universal 'formation number' as in the above studies. This is probably due to the fact that in a confined jet the proximity of the walls dominates the overall dynamics.

Following the 'pinch-off' of structure A, a series of detached vortices forms by the time the flow rate is close to its maximum value. A typical example of the flow at this time is shown in figure 6(*d*) where the structure B (indicated by the arrow) is clearly visible behind A. The generation of the above structures is probably the result of an instability of the shear layers. In particular, on inspecting a series of animations and velocity time series generated from the DNS database, small oscillations were observed
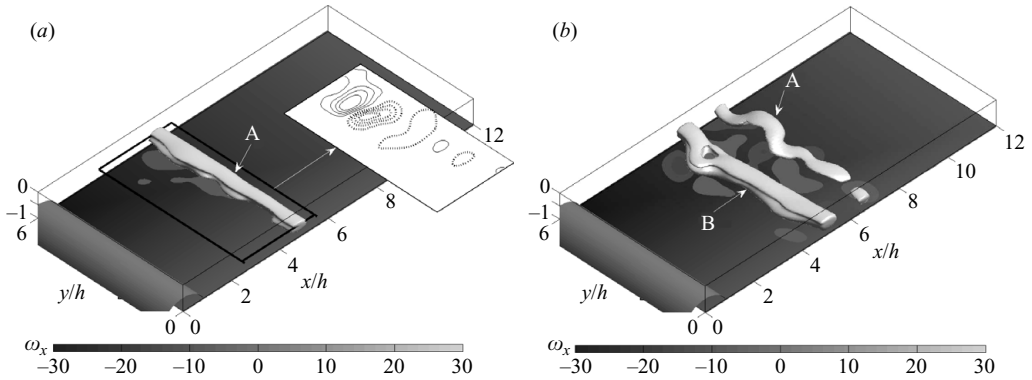
FIGURE 8. Early stages of the formation and evolution of coherent spanwise structures in case 1 visualized by iso-surfaces of Q. The time instants for (a) and (b) correspond to the ones shown in figures 6(c) and 6(d) respectively. Selected contours of $(dU/dy)h/U_m$ are shown at a slice through the vortex in (a). Values of contours are ± 0.1, ± 0.2, ± 0.3 and ± 0.4, with negative values represented by dotted lines. Only the bottom half of the channel is shown and filled iso-contours of $\omega_x h/U_m$ are plotted on the wall.

in the shear layers as early as $t/T \sim 0.2$. They gradually increased in amplitude and eventually lead to the local collapse of the recirculation bubble and the formation of the detached structures shown in figure 6. A similar Kelvin–Helmholtz-like instability has been observed in impulsively accelerating jets (Rosenfeld *et al.* 1998; Gharib *et al.* 1998) and has been shown to affect the evolution of the detached leading vortex described earlier (Zhao, Frankel & Mongeau 2000). Sherwin & Blackburn (2005) also suggested that the jet shear layers are most likely subject to a convective instability, which was based on the high receptivity of their DNS to a well-defined frequency band, as well as the absence of vortex formation in their unforced simulations.

Following the initial formation of these quasi-two-dimensional detached vortical structures, we looked into the details of their spatio-temporal evolution and their role in the initiation of turbulence. Figures 8(a) and 8(b) show snapshots of the instantaneous flow structures at two instances in time (the same case as in figures 6c and 6d respectively). Isosurfaces of the second invariant of the velocity gradient tensor, or Q-criterion (see Hunt, Wray & Moin 1988), on the lower half of the channel are shown to visualize the vortical structures, while contours of the streamwise vorticity are plotted on the bottom wall. Figure 8(a) shows that the first vortex to detach from the shear layer (indicated by A in the figures) is initially very coherent and uniform along the span of the channel, and as it is convected downstream, it undergoes a three-dimensional instability and evolves into what resembles a Λ-type structure (see figure 8b). The vortices that subsequently form behind structure A (see structure B in the same figure) undergo a similar evolution. For all cases listed in table 1, the above appears to be the primary mechanism that is responsible for the reorientation of spanwise vorticity into streamwise vorticity, which will eventually lead to the formation of streamwise vortex packets. This conjecture is consistent with the presence of strong spanwise gradients of the streamwise velocity (see the inset in figure 8a near $y/h = 5$) during the early stages of this process, indicating that the dominant production term in the transport equation for streamwise vorticity is $\omega_y \partial U/\partial y$ (this was subsequently verified by direct computation of all stretching terms in the above transport equation). Such mechanisms for reorientation of spanwise vorticity are common in numerous free-shear and wall-bounded flows (see for example Lasheras,
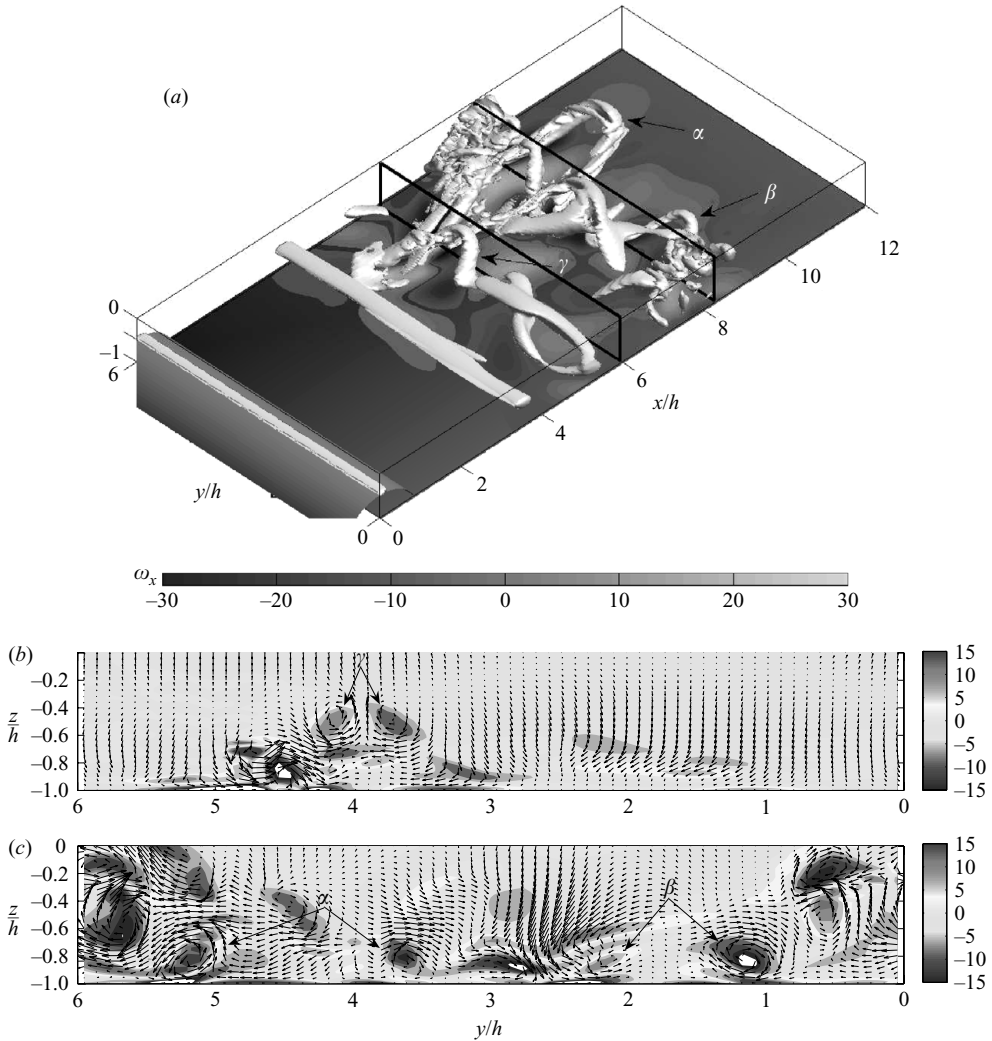
FIGURE 9. (*a*) A snapshot of the dominant coherent structures in case 1 visualized by iso-surfaces of Q, shortly before the maximum flow rate ($t/T = 0.4$). Only the bottom half of the channel is shown and iso-contours of streamwise vorticity, $\omega_x h/U_m$ are plotted on the wall. (*b*, *c*) Instantaneous distribution of $\omega_x h/U_m$ at the two (y, z)-planes indicated on (*a*). In-plane, instantaneous velocity vectors are also shown. Arrows in all parts of the figure point to the hairpin-like structures, α, β and γ in (*a*)
.

Cho & Maxworthy 1986; Heist, Hanratty & Na 2000). The observed asymmetry in the spanwise gradients and their resulting deformation is probably due to small-scale disturbances that remain in the post-stenotic region from previous cycles.

As this instability evolves, the initially quasi-two-dimensional rollers lose most of their spanwise coherence, and their subsequent interaction with the wall generates packets of hairpin-like vortices. Figure 9(*a*) shows selected isosurfaces of the Q criterion at $t/T = 0.4$ and velocity vectors on two (y, z)-planes across the wall. As can be seen, the downstream edge of the structures shown in the figure consists of pairs of horseshoe-like vortices, reminiscent of the near-wall structures seen in turbulent boundary layers. These vortices are made up of two legs that are almost parallel and
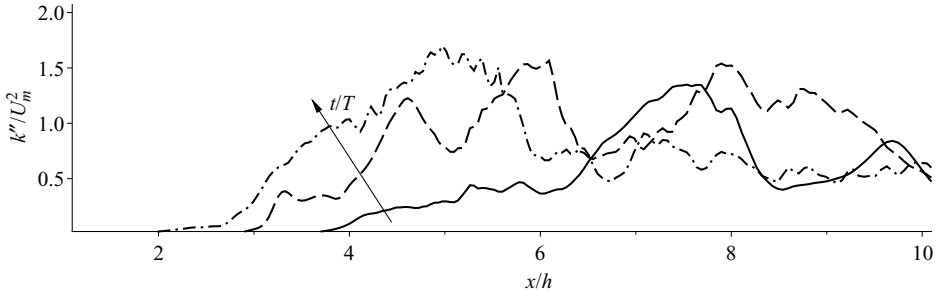
FIGURE 10. Spanwise-averaged turbulent kinetic energy (case 1). Streamwise variation at $z/h = -0.5$ at three instances in the pulsatile cycle: ———, $t/T = 0.4$; - - -, $t/T = 0.45$; — · —, $t/T = 0.5$.
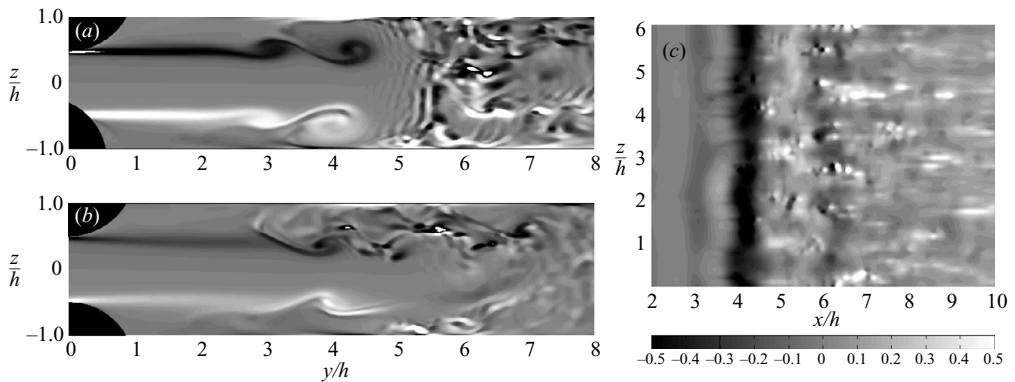

FIGURE 11. Iso-contours of instantaneous spanwise vorticity ($\omega_y h/U_m$) at two instances during the deceleration in case 1; (a) $t/T = 0.58$, (b) $t/T = 0.77$ and (c) plot of C_f on the bottom wall at $t/T = 0.58$.

close to the wall, and a head region that extends downstream and away from the wall. Spanwise cuts through the flow reveal pairs of counter-rotating streamwise vortices that correspond to the legs of the hairpin vortices (structures α, β and γ indicated by arrows in figure 9). It is evident that these hairpin vortices are the direct evolution of the detached structures shown in figure 8. Furthermore, these hairpin-like structures induce other streamwise vortical structures, creating a highly three-dimensional and random flow field, which starts to generate disturbances within the structures upstream.

As the flow rate starts to decrease ($t/T \sim 0.5$) the disturbances generated from the evolution and breakdown of the above-mentioned vortical structures slowly propagate upstream. This can be clearly seen in figure 10, where the variation along x of the spanwise-averaged turbulent kinetic energy, k, is shown at three instances in the pulsatile cycle. As time increases, a disturbance front travels upstream approaching $x/h = 2$. The dynamics of the shear layers, which now have a shedding frequency of approximately twice the one observed for $t/T < 0.5$, also changes substantially. Figure 11 shows contours of the instantaneous spanwise vorticity at an (x, z)-plane, located approximately at channel centre-span, at two characteristic instants during the period $0.5 < t/T < 1.0$. At $t/T \sim 0.58$ (see figure 11a) a distinct roll-up of the shear layer is observed at $x/h = 4$. In contrast to figure 6, a well-defined shear layer extends only up to $x/h = 4$, beyond which only smaller elongated structures can be distinguished across the channel. This is also reflected on the instantaneous
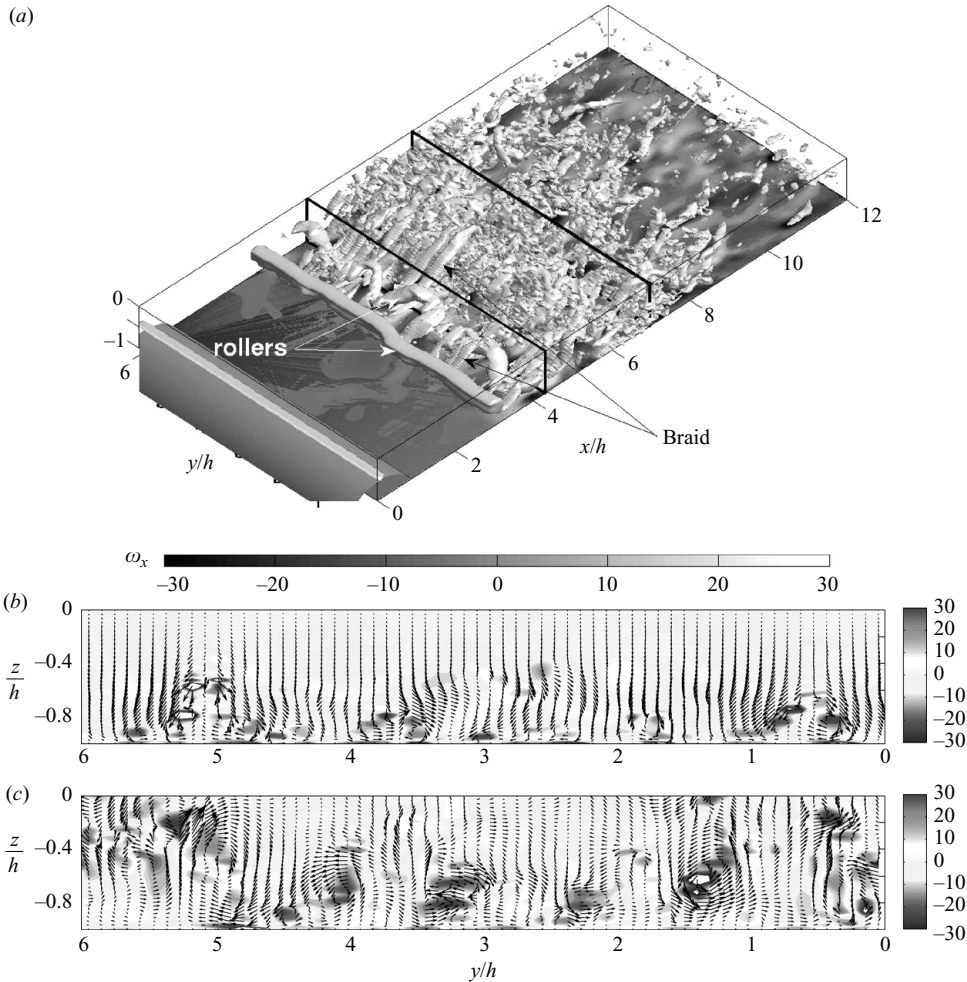
FIGURE 12. (*a*) A snapshot of the dominant coherent structures in case 1 visualized by iso-surfaces of Q at $t/T = 0.58$. Only the bottom half of the channel is shown and iso-contours of streamwise vorticity, $\omega_x h/U_m$ are plotted on the wall. (*b*, *c*) Instantaneous distribution of $\omega_x h/U_m$ at the two (y,z)-planes in the braid regions marked on (*a*): (*b*) $x/h = 4$, (*c*) $x/h = 7$.

skin friction coefficient (see figure 11*c*), which shows that the vortices shed by the shear layer quickly lose their spanwise coherence as they convect beyond $x/h > 5$. In addition, smaller structures originating from breakups having occurred downstream can be clearly seen inside the recirculation bubble in figure 11(*b*), where they become entrained by or merge with the shear layers. This points to the fact that shear layer instability is no longer convective but it attains a rather absolute nature.

A snapshot of the characteristic coherent structures during this part of the cycle is shown in figure 12. A quasi-two-dimensional spanwise roller can be seen at $x/h \sim 3$, and just downstream another roller undergoes a three-dimensional instability. Between the two rollers, there is a 'braid' region where several counter-rotating rib vortices exist. The strength of these vortices is better illustrated in figure 12(*b*, *c*) where instantaneous isolines of streamwise vorticity, ω_x, at (y,z)-planes located in the braid regions are shown. The overall picture resembles that of a mixing layer, indicating that the shear layers during this part of the cycle undergo both Kelvin–Helmholtz-type, and three-dimensional braid instabilities.
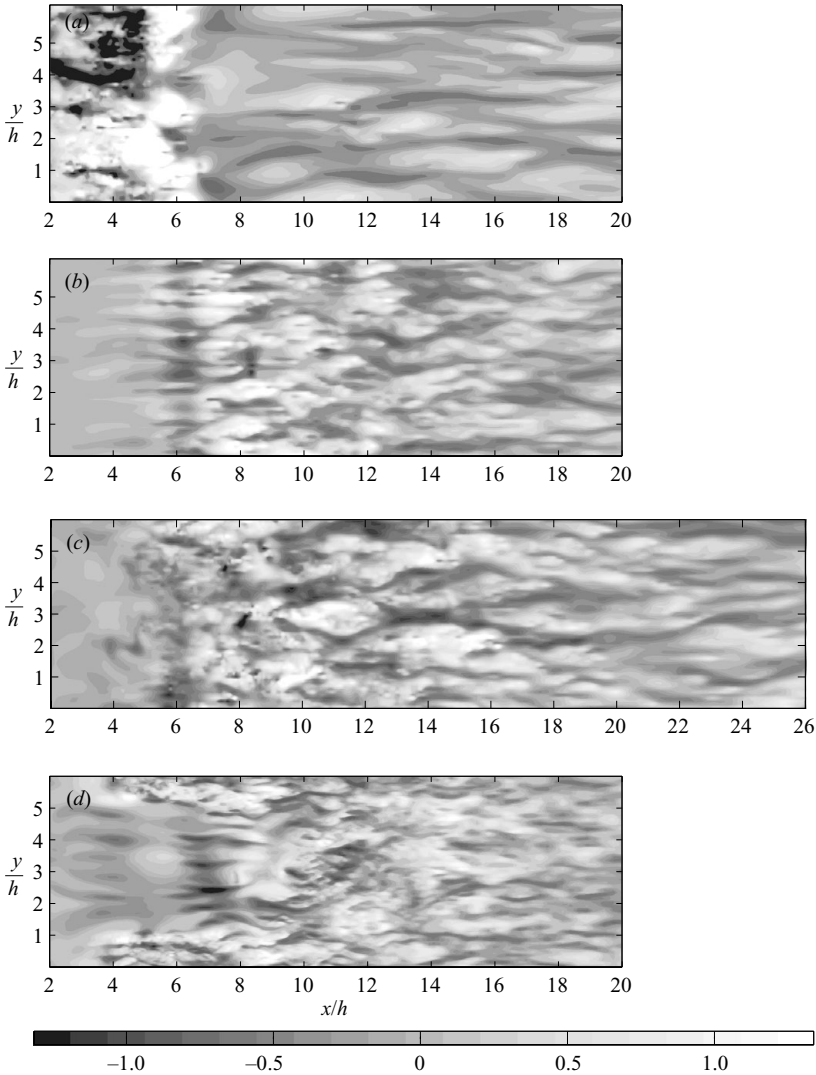
FIGURE 13. Iso-contours of the instantaneous velocity fluctuations, u''/U_m, at an (x, y)-plane above the bottom wall $(z/h = 0.1)$ at a characteristic instances after the maximum flow rate for each case: (a) case 1; $t/T = 0.75$, (b) case 2; $t/T = 0.75$, (c) case 3; $t/T = 0.5$ and (d) case 4; $t/T = 0.75$.

The initiation of the shear layer roll-up and duration of the subsequent vortex shedding depends on the time scale of the imposed oscillations. In particular, as the reduced velocity, U_{red}, increases, the vortex shedding begins earlier in the cycle and lasts for a greater part of the cycle (see figure 7). In all cases though, it is evident that for approximately half or more of the pulsatile cycle, the confined jet constantly generates a series of quasi-two-dimensional spanwise-coherent structures and streamwise rib vortices that through various instability mechanisms evolve into hairpin-like vortices propagating on the wall and are responsible for most of the momentum transport near the wall. The spatial evolution of these turbulent-like structures can be traced by examining the contours of the instantaneous velocity fluctuations, u'' at an (x, y)-plane near the wall. In figure 13, snapshots of u'' for all cases are shown at an (x, y)-plane
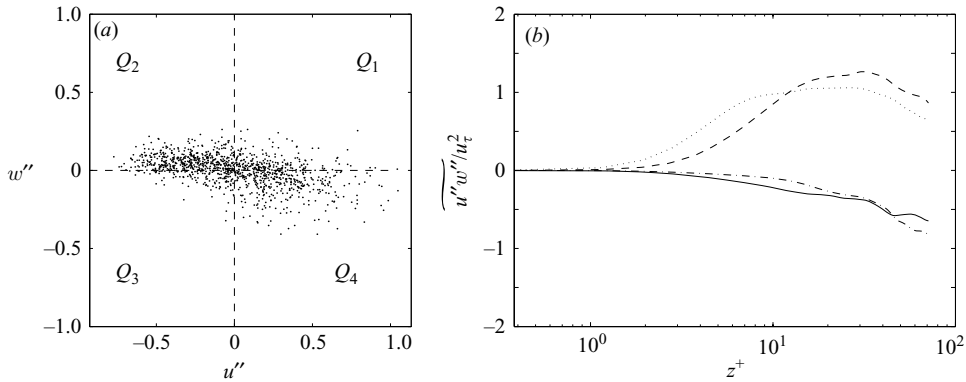
FIGURE 14. (*a*) Scatter plot of u''/U_m, w''/U_m events in case 1 at location $x/h = 17$ and $z/h = 0.1$. (*b*) The quadrant decomposition of the Reynolds shear stress, $\widetilde{u''w''}$, across the channel at the $x/h = 17$. ———, Q_1: first quadrant ($u'' > 0$, $w'' > 0$); – – –, Q_2: second quadrant ($u'' < 0$, $w'' > 0$); — · —, Q_3: third quadrant ($u'' < 0$, $w'' < 0$); ········, Q_4: fourth quadrant ($u'' > 0$, $w'' < 0$). For both parts $t/T = 0.025$.

located at $z/h = 0.1$ at a time just after the maximum flow rate. Intense velocity fluctuations appear near the reattachment line in each case, which can be correlated with the three-dimensional instabilities of the spanwise rollers. In all cases, short 'streaks' of negative and positive u'' fluctuations can be identified shortly after the reattachment point. These short streaks merge as they evolve downstream, forming structures that are reminiscent of the high- and low-speed streaks seen in turbulent boundary layers. We have also looked at different instances during the cycle and qualitatively similar patterns are observed as long as vortex shedding takes place. However, the evolution of these structures in time is different as U_{red} changes, which is discussed later in the paper.

To better illuminate the effect of these structures on the momentum transport dynamics, the quadrant decomposition of $\widetilde{u''w''}$ (see Wallace, Eckelmann & Brodkey 1972) across the channel is shown for case 1 in figure 14. Results are shown for a characteristic location at $x/h = 12$, although statistics at other downstream locations are qualitatively similar. Clearly, near the wall the second ($u'' < 0$, $w'' > 0$) and fourth quadrant ($u'' > 0$, $w'' < 0$) contributions are dominant, which is consistent with the presence of streaks. This is also reflected in the scatter plot of u'' and w'' events shown in figure 14(*a*). On moving away from the wall, more and more negative streamwise fluctuations are correlated with positive wall-normal fluctuations. In a qualitative sense this behaviour is very similar to the quadrant analysis of a turbulent channel flow, where sweep events dominate the viscous layer and ejections events gradually overwhelm them away from the wall. In the present case, however, the wall-normal location where sweep events equal the ejections does not remain constant throughout the cycle, and appears to move closer to the wall as the flow decelerates. In addition, the exact contributions to the Reynolds shear stress vary with downstream distance as turbulent structures develop past the reattachment point.

4.3. *Statistics and budgets*

In the previous section, we identified the vortical structures that dominate the dynamics of the flow in the shear layer and in the near-wall region after the mean reattachment point. Next, we will examine the effect that these structures have on the
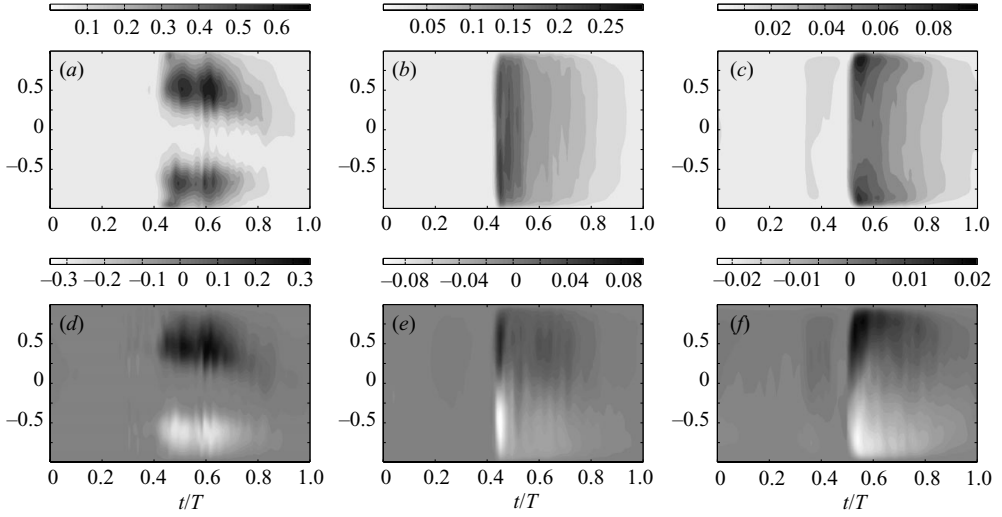
FIGURE 15. Contours of $\tilde{k}/U_m^2$ for (a) $x/h=4$, (b) $x/h=12h$, and (c) $x/h=20$, and $\widetilde{u''w''}/U_m^2$ for (d) $x/h=4$, (e) $x/h=12h$, and (f) $x/h=20$ for case 1 plotted in t/T versus z/h space.

phase-averaged statistics and turbulence kinetic energy production, dissipation and transport in the channel. Figure 15 shows the phase-averaged turbulent kinetic energy, k, and the Reynolds shear stress, $\widetilde{u''w''}$, normalized by the 'local' bulk velocity, $\tilde{U}_b$, in the pulsatile cycle and the half-channel height. To illuminate the spatio-temporal behaviour of these quantities, contours in z/h versus t/T space are shown at three characteristic streamwise locations: one before ($x/h=4$), and two after ($x/h=12$ and $x/h=20$) the mean reattachment point.

Very distinct patterns can be identified in the evolution of k and $\widetilde{u''w''}$ between the different streamwise stations. In particular, shortly before maximum flow rate there is a sudden burst in the levels of turbulent kinetic energy at $x/h=4$. Most of it, however, is confined around the shear layers with relatively low levels near the walls, and negligible levels near the centreline. The levels of turbulent kinetic energy remain elevated for the first half of the deceleration, after which they gradually drop to very low levels and move towards the centreline as the jet becomes asymmetric. Finally, as the flow rate increases, turbulence activity in the channel remains negligible. At $x/h=12$ (downstream of the mean reattachment location), the turbulent kinetic energy appears in a sudden burst prior to the peak flow rate, and is distributed uniformly across the channel, with high levels both near the wall and the core. The levels gradually decay prior to the minimum flow rate, and no pronounced asymmetries can be identified at this location. Further downstream of the reattachment point at $x/h=20$, peaks of the turbulent kinetic energy are only observed close to the walls, with a significant decay as one moves towards the centreline. The maximum levels of turbulent kinetic energy are sustained between $t/T=0$ and $t/T=0.1$, although the relative peaks near the wall still remain throughout most of the deceleration. As the flow rate increases, turbulent kinetic energy remains low, indicating that the flow during this part of the cycle tries to relaminarize throughout the channel.

Qualitatively similar patterns can be traced in the evolution of the turbulent Reynolds shear stress at the same downstream locations. Although $\widetilde{u''w''}$ is not the only component contributing to the production of turbulent kinetic energy, it is dominant in the regions of interest and gives a good indication of the regions

where turbulence is 'active'. In particular, most of the turbulence production takes place around the shear layers at $x/h = 4$ from $t/T = 0.40$ to $t/T = 0.80$. As the flow reattaches, the levels of $\widetilde{u''w''}$ are more uniform across the channel, while further downstream at $x/h = 20$ peaks of $\widetilde{u''w''}$ are observed near the wall. This suggests that after the mean reattachment point the near-wall region dynamics resemble those of turbulent boundary layers, while in the core turbulence is simply convected from upstream and is dissipated.

It is also important to point out the difference in the levels of turbulent kinetic energy and Reynolds shear stress as one moves from the shear-layer-dominated region ($x/h \sim 4$), to a station downstream of the mean reattachment point ($x/h \sim 12$), where boundary-layer-like behaviour is observed. Using simple scaling arguments, the intensity of the turbulent activity present in the shear layers at the former station cannot be naturally sustained in magnitude in an equilibrium turbulent wall layer. Therefore in addition to the temporal decay of the turbulent kinetic energy and Reynolds shear stresses observed at each location due to the decreasing Reynolds number, there is a spatial decay of the above quantities as the nature of turbulence transitions from that of a shear layer to that of a wall layer.

To better understand how turbulent kinetic energy is produced, dissipated, and transported in the post-stenotic area, we examined the budgets of the phase-averaged turbulent kinetic energy governed by the following equation:

$$\frac{\partial \tilde{k}}{\partial t} = \underbrace{-\widetilde{u_i''u_j''}\frac{\partial \widetilde{U_i}}{\partial x_j}}_{P_k} - \underbrace{\frac{1}{Re}\widetilde{\frac{\partial u_i''}{\partial x_j}\frac{\partial u_j''}{\partial x_i}}}_{\epsilon_k} - \underbrace{\widetilde{U_j}\frac{\partial \tilde{k}}{\partial x_j}}_{C_k} - \underbrace{\frac{\widetilde{\partial p''u_j''}}{\partial x_j}}_{\Pi_k} + \underbrace{\frac{1}{Re}\nabla^2 \tilde{k}}_{D_k} - \underbrace{\frac{\partial \widetilde{u''k}}{\partial x_j}}_{T_k} \qquad (4.1)$$

where $k = \frac{1}{2}u_i''u_i''$. The term on the left-hand side is the phase-averaged rate of change ($\partial k / \partial t$) of the turbulent kinetic energy. On the right-hand side, the first and second terms are usually defined as the production (P_k) and dissipation (ϵ_k) of k, and are the only terms that add or remove energy. The last four terms on the right-hand side represent transport of turbulent kinetic energy by the phase-averaged flow field (C_k), pressure velocity correlations (Π_k), diffusion (D_k), and turbulent transport (T_k) respectively. These terms can be written in conservative form and are responsible for redistributing k. Figure 16 shows the variation of these terms across the channel at two instances during the cycle and at three locations representative of the distinct flow features that exist downstream of the stenosis: one within the shear layer ($x/h = 4.8$), one shortly after the mean reattachment point ($x/h = 9.2$), and one in reattached wall layer ($x/h = 17.0$). For clarity Π_k, D_k and T_k have been lumped together as the total transport of turbulent kinetic energy.

Near the maximum flow rate at the station closest to the stenosis (see figure 16a), the turbulent kinetic energy is predominantly produced within the shear layers as indicated by the shape of P_k, which peaks at $z/h \pm 0.5$, and then goes to zero towards the centre and the walls of the channel. Only a small part of the turbulent kinetic energy produced at the shear layers, however, is being dissipated: ϵ_k is just a small fraction of the production term except for a small area very close to the wall. Instead, most of the energy produced is being transported away from the shear layers and towards the centre of the channel (mainly by T_k) and the walls (mainly by D_k and Π_k) where it is balanced by ϵ_k. The remaining energy in the core of the channel is then convected by C_k.

After the flow reattaches, the energy balance changes dramatically. On one hand, there is no production of turbulence away from the wall, as indicated by P_k in
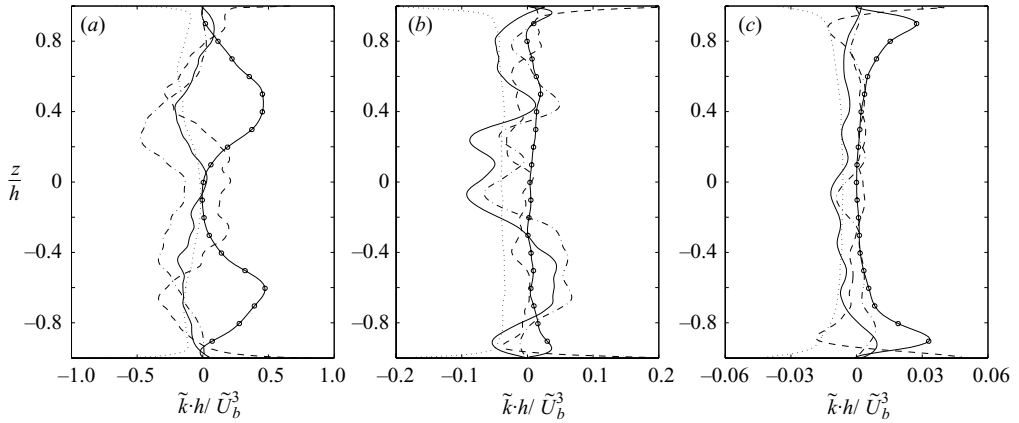
FIGURE 16. Budgets of the phase-averaged turbulent kinetic energy for case 1 at $t/T = 0.5$ for three downstream locations (a) $x/h = 4.8$, (b) $x/h = 9.2$, and (c) $x/h = 17.0$. The terms are shown as follows: $\bigcirc$, P_k; $\cdots\cdots$, ϵ_k; $---$, T_k; ———, C_k; —·—, $\partial k/\partial t$.

figure 16(b), and the rate at which turbulent kinetic energy is transported across the channel is relatively small (as shown by T_k). The dominant terms for most of the channel are now the dissipation, ϵ_k, and the convection, C_k, which at this location is predominantly in the streamwise direction. On the other hand, the relative peaks in P_k and T_k near the wall, suggest that a 'turbulent-like' layer starts to develop. This is consistent with the presence of the streamwise-oriented vortices discussed in the previous section, which transport momentum across the channel and sustain turbulent activity near the wall. As indicated by the balance of the different terms, this near-wall flow is almost independent of the turbulent activity in the core, which consists of decaying, 'inactive', fluctuations.

Further downstream of the reattachment point, the turbulent kinetic energy budget shown in figure 16(c) resembles more that of a turbulent wall-bounded flow. There is a clear peak in P_k near the wall while it decays quickly to negligible levels away from it. Transport and dissipation are also dominant near the wall, as found in a classical turbulent channel flow – although important differences exist between the two. First of all, the convection C_k and rate of change of turbulent kinetic energy $\partial k/\partial t$ are not zero in our case, because the flow is still developing. Second, away from the wall the dissipation, ϵ_k, is orders of magnitude larger than production, P_k. Finally, the similarity to classical equilibrium wall-bounded flow was investigated by renormalizing the different terms in the budget equations using the local u_τ and ν (not shown here). Although the overall magnitude of the different terms (especially production and dissipation near the wall) is close to that found in low-Reynolds-number channel flow, the differences discussed above still remain. Given the superficial similarity of these regions to classical wall-bounded turbulent layers, from now on we will refer to them as 'synthetic' turbulent boundary layers.

Throughout the deceleration phase, it was found that as long as energy is fed to the flow through the shear layer instability, the budgets of turbulent kinetic energy remain qualitatively similar (see figure 17). The main difference during the late deceleration stage is associated with the asymmetry of the jet, which causes the peaks of P_k at the shear layers to shift accordingly as shown in figure 17(a). This asymmetry, however, does not seem to significantly affect the energy balance downstream of the reattachment point as the turbulent kinetic energy contained in the wake of the
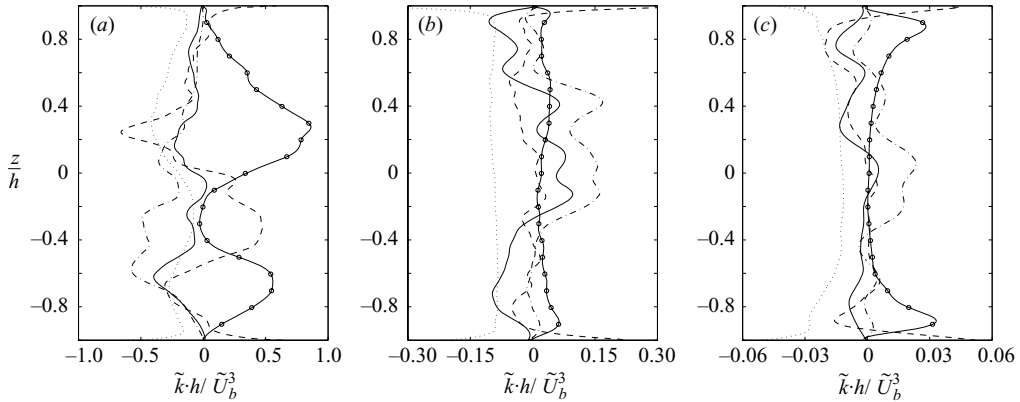
FIGURE 17. As figure 16 but at $t/T = 0.75$.

jet is passive. In addition, the dimensional values of of the turbulent kinetic energy production, dissipation and transport throughout the channel decrease by an order of magnitude.

From the above analysis it is clear that the turbulent activity is driven by the dynamics of the shear layer, which is also consistent with the observations of the instantaneous dynamics of the flow. In particular, within the wall layer downstream of the reattachement point, the turbulent kinetic energy production is mostly sustained by the evolution/interaction of large vortical structures that originate from the shear layers. Even for the highest values of the Reynolds number we considered (case 5), as the shear layers weaken near the minimum flow rate ($t/T \sim 1.0$), vortex shedding stops and the near-wall turbulence cannot be sustained. This is evident in figure 18, where the time evolution of the near-wall maxima of the phase-averaged turbulent kinetic energy and its production at a location within the region of the 'synthetic' turbulent boundary layers (approximately $14h$ past the mean reattachment point), is shown. For the cases with the higher values of reduced velocity ($U_{red} \geqslant 26.5$), the transition to a turbulent-like regime downstream of the reattachment point appears in a burst, as indicated by a dramatic spike in the levels of the turbulent kinetic energy and the finite values of the production term. Specifically, the duration of the production events corresponds to the duration of active structure formation observed within the free shear layers. For example, in case 3, dominant production begins at $t/T = 0.5$ and decays to zero approximately at $t/T = 0.95$. This corresponds closely to the active structure formation duty cycle of the shear layer of approximately 0.45. For cases 4 and 5 the duty cycles are 0.68 and 0.60 respectively, which also compare well with the production durations shown in figure 18. The case with $U_{red} = 6.6$ (case 2), however, is the exception and does not fit the above pattern. Finite values of production of kinetic energy are found throughout the duration of the cycle, whereas the active duration of the shear layer duty cycle is only 0.35. This is most likely because the comparatively small mean convection velocity enables the relatively few active structures to remain in the near-wall region for the majority of the cycle.

5. Summary

In the present paper, DNS of transitional pulsatile flow in a channel with a constriction have been presented. Parallel to the DNS, an experiment designed to validate the computations and guide the development of proper inflow boundary
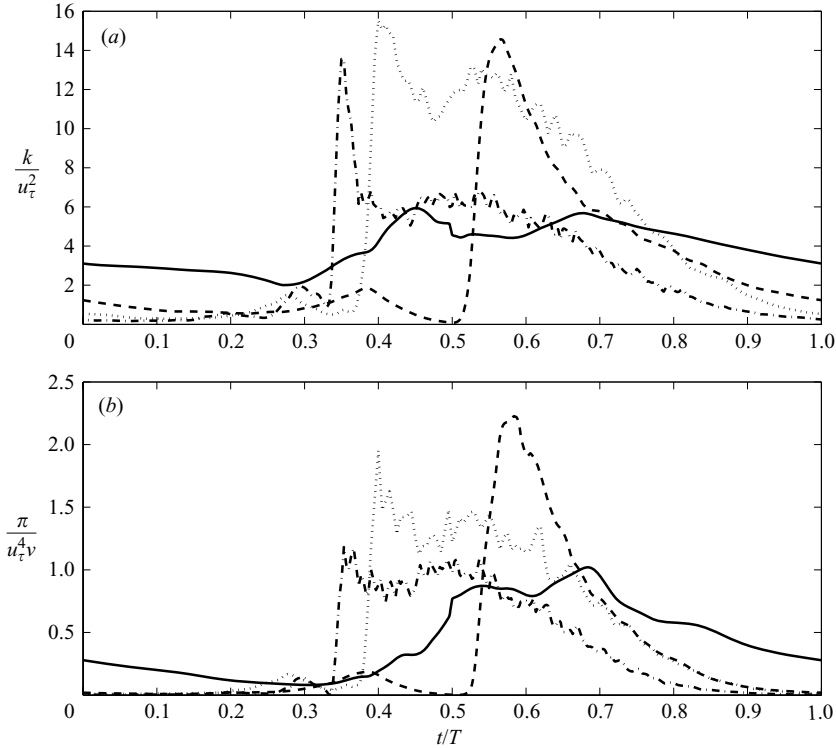
FIGURE 18. (a) Near-wall maxima of the phase-averaged turbulent kinetic energy and (b) turbulent kinetic energy production as a function of time at $x/h = 14$ downstream of the mean reattachment point: ——, case 2 ($Re = 600$, $U_{red} = 6.6$); - - -, case 3 ($Re = 600$, $U_{red} = 26.5$); — · —, case 4 ($Re = 600$, $U_{red} = 106.2$); ········, case 5 ($Re = 1200$, $U_{red} = 53.1$).

conditions was conducted. The measurements showed that during part of the pulsatile cycle the flow upstream of the stenosis undergoes a transition from a laminar to a 'disturbed-laminar' state as a result of an instability associated with the inflection points in the velocity profiles. We found that reproducing this state is important to properly capture transition downstream of the constriction. In general, the DNS results were in very good agreement with the experiment, and the formation and instability of the confined jet through the stenosis was captured accurately. In addition, the phase-averaged velocity statistics of the streamwise velocity follow very closely those from the experiment.

Having established the validity of the simulations, the instantaneous flow dynamics were investigated. It was found that the quasi-two-dimensional vortical structures originating from the initial stages of a shear layer instability undergo three-dimensional instabilities as they interact with the wall and form Λ-type structures. The evolution of these structures results in the formation of packs of hairpin-like vortices downstream of the reattachment point. After the peak flow rate, and as disturbances from this turbulent-like front propagate upstream, the shear layer dynamics change, and a distinct roll-up could be observed. In particular, the structures near the stenosis were reminiscent of those found in a typical mixing layer, with the existence of spanwise rollers undergoing three-dimensional instabilities and rib vortices in the braid areas. Despite the differences, both stages of the shear layer instability essentially

reorient the spanwise vorticity into the streamwise direction, constantly feeding the reattached wall layer with turbulent-like structures. Further downstream, the footprint of these structures on the streamwise velocity fluctuations indicates the presence of high- and low-speed streaks. We found this mechanism to be universal in the parametric range investigated.

Finally, we also presented phase-averaged statistics of the velocity field and turbulent kinetic energy budgets. These results indicate that the overall turbulent activity is driven by the dynamics of the shear layer, which is also consistent with the observations of the instantaneous dynamics of the flow. Turbulent kinetic energy is produced at the shear layers and is transported towards the core of the channel, where it remains 'passive' and decays as it is convected downstream. Production of turbulent kinetic energy in the wall layer further downstream, although a dynamically different process, is in practice sustained by the evolution/interaction of large vortical structures that originate from the shear layers.

Finally the effect of the Reynolds number and the reduced velocity on the near-wall turbulence was discussed. It was observed that by increasing the Reynolds number the shear layers instability (and consequently turbulence production) is initiated earlier in the cycle. However for the cases with higher U_{red} the turbulence activity could not be sustained during the entire cycle. It is observed that as the time scale of the imposed oscillations increases dissipation has more time to act and completely kills the turbulent structures present in the reattached wall region. Only for the case with $U_{red} = 6.6$ is turbulent kinetic energy sustained during the entire cycle.

Appendix. Phase-average operators

Because the LDV records data samples with random arrival times as a result of the stochastic nature of the seeding particles, the procedure for computing phase-averaged statistics outlined in §3 approximates these definitions. In particular, the experiments were only conducted in the midplane of the channel ($L_y = 0$) and the period was divided into 90 time interval bins. The phase-average streamwise velocity $\tilde{U}(t)$ was calculated by finding the mean of all velocities whose arrival time was within the specified interval. To correct for the velocity bias inherent in turbulent LDV statistics (see, for example, Adrian 1996), the velocities were weighted by their residence time a, which is the total time a particle remains within the focus area of the laser beam. The averaging yielded by this discrete variation of equation (3.2) will be denoted by $\langle \rangle$, as shown below:

$$\langle f \rangle (x, z, t) = \frac{\sum_{n=1}^{N} \sum_{(t+nT)-\Delta t/2}^{(t+nT)+\Delta t/2} a(x, y, z, t)\, f(x, y, z, t)}{\sum_{n=1}^{N} \sum_{(t+nT)-\Delta t/2}^{(t+nT)+\Delta t/2} a(x, y, z, t)} \tag{A 1}$$

where $a(x, y, z, t)$ is the residence time of a particle, $\Delta t = T/90$, and summation is over all particles arriving between $t - \Delta t$ and $t + \Delta t$. In an analogous manner the

phase-averaged second-order moment was calculated as

$$\langle f'' f'' \rangle (x, z, t) = \frac{\displaystyle\sum_{n=1}^{N} \sum_{(t+nT)-\Delta t/2}^{(t+nT)+\Delta t/2} a(x, y, z, t)(f(x, y, z, t) - \langle f \rangle)^2}{\displaystyle\sum_{n=1}^{N} \sum_{t-\Delta t/2}^{t+\Delta t/2} a(x, y, z, t)}. \qquad (A\,2)$$

Obviously, as Δt decreases equations (A 1) and (A 2) converge to (3.2) and (3.3) provided there are enough samples within each bin. In the experiment, averages were conducted over approximately $N = 100$ periods. To mimic the above operator in the DNS, whenever comparing with the experimental data, the velocity signal was also divided into 90 bins and local time averages were computed.

REFERENCES

ADRIAN, R. J. 1996 Laser velocimetery. In *Fluid Mechanics Measurements* (ed. R. J. Goldstein). Taylor & Francis.

AHMED, S. A. & GIDDENS, D. P 1984 Pulsatile poststenotic flow studies with laser doppler anemometry. *J. Biomech.* **17**, 695–705.

BALARAS, E. 2004 Modeling complex boundaries using an external force field on fixed Cartesian grids in large-eddy simulations. *J. Fluid Mech.* **33**, 375–404.

BERATLIS, N., BALARAS, E., PARVINIAN, B. & KIGER, K. 2005 A numerical and experimental investigation of transitional pulsatile flow in a stenosed channel. *J. Biomech. Engng* **127**, 1147–1157.

BERGER, S. A. & JOU, L. D. 2000 Flows in stenotic vessels. *Annu. Rev. Fluid Mech.* **32**, 347–382.

CASSANOVA, R. A. & GIDDENS, D. P. 1978 Disorder distal to modeled stenoses in steady and pulsatile flow. *J. Biomech.* **11**, 441–453.

DAVIES, P. F., REMUZZI, A., GORDON, E. J., DEWEY, C. F. & GIMBRONE, M. A. 1986 Turbulent Fluid Shear Stress Induces Vascular Endothelial Cell Turnover in vitro. *Proc. Natl Acad. Scie. USA* 83, No. 7, pp. 2114–2117.

GHARIB, M., RAMBOD E. & SHARIFF K. 1998 A universal time scale for vortex ring formation. *J. Fluid Mech.* **360**, 121–140.

HEIST, D. K., HANRATTY, T. J. & NA, Y. 2000 Observations of the formation of streamwise vortices by rotation of arch vortices. *Phys. Fluids* **12**, 2965–2975.

HUNT J. C. R., WRAY, A. A. & MOIN, P. 1988 Eddies, streams and convergence zones in turbulent flows. *Center for Turbulence Research, Proceedings of the Summer Program 1988*, p. 193.

KHALIFA, A. M. A. & GIDDENS, D. P. 1978 Analysis of disorder in pulsatile flows with application to poststenotic blood velocity measurement in dogs. *J. Biomech.* **11**, 129–141.

KHALIFA, A. M. A. & GIDDENS, D. P. 1981 Characterization and evolution of poststenotic flow disturbances. *J. Biomech.* **14**, 279–296.

KIM, J., MOIN, P. & MOSER, R. 1987 Turbulence statistics in fully developed channel flow at low Reynolds number. *J. Fluid Mech.* **117**, 133–166.

KU, D. N. 1997 Blood flow in arteries. *Annu. Rev. Fluid Mech.* **29**, 399–434.

LASHERAS, J. C., CHO, J. S. & MAXWORTHY, T. 1986 On the origin and evolution of streamwise vortical structures in a plane, free shear layer. *J. Fluid Mech.* **172**, 231–258.

LIEBER, B. B. & GIDDENS, D. P. 1990 Post-stenotic core flow behavior in pulsatile flow and its effects on wall shear stress. *J. Biomech.* **23**, 597–605.

LU, P. C., GROSS, D. R. & HWANG, N. H. C. 1980 Intravascular pressure and velocity fluctuations in pulmonic arterial stenosis. *J. Biomech.* **13**, 291–300.

MAYO, W. 1978 Spectrum measurements with laser velocimeters. In *Dynamic Measurements in Unsteady Flows; Proc. Dynamic Flow Conf. Marseille, France, 11–14 September 1978 and Baltimore, USA; Denmark 18–21 September 1978*, pp. 851–868.

MITTAL, R., SIMMONS, S. P. & UDAKUMAR, H. S. 2001 Application of large-eddy simulation to the study of pulsatile flow in a modeled arterial stenosis. *J. Biomech. Engng* **123**, 325–332.

OJHA, M., RICHAR, S. C. C., JOHNSTON, K. W. & HUMMEL, R. L. 1984 Pulsatile flow through constricted tubes: an experimental investigation using photochromic tracer methods. *J. Fluid Mech.* **203**, 173–197.

ORLANSKY, I. 1974 A simple boundary condition for unbounded hyperbolic flows. *J. Comput. Phys.* **21**, 251–269.

PANTON, R. 1996 *Incompressible Flow*, 2nd edn. John Wiley & Sons.

POELMA, C. 2004 Experiments in particle-laden turbulence. PhD Thesis, Technische Universiteit Delft.

POELMA, C., WESTERWEEL, J. & OOMS, G. 2006 Turbulence statistics from optical whole-field measurements in particle-laden turbulence. *Exps. Fluids* **40**, 663.

ROGALLO, R. S. 1981 Numerical experiments in homogeneous turbulence. *NASA Tech. Mem.* 81315.

ROSENFELD, M., RAMBOD E. & GHARIB, M. 1998 Circulation and formation number of laminar vortex rings. *J. Fluid Mech.* **376**, 297–318.

RYVAL, J., STRAATMAN, A. G. & STEINMAN, D. A. 2004 Two-equation turbulence modeling of pulsatile flow in a stenosed tube. *J. Biomech. Eng.* **126**, 625–635.

SCOTTI, A. & PIOMELLI, U. 2001*a* Numerical simulation of pulsating turbulent channel flow. *Phys. Fluids* **13**, 1367–1384.

SCOTTI, A. & PIOMELLI, U. 2001*b* Turbulence models in pulsating flows. *AIAA Paper.* 2001-0729.

SHERWIN, S. J. & BLACKBURN, H. M. 2005 Three-dimensional instabilities and transition of steady and pulsatile axisymmetric stenotic flows. *J. Fluid Mech.* **533**, 297–327.

SIOUFFI, M., DEPLANO, R. & PELISSIER, R. 1998 Experimental analysis of unsteady flows through a stenosis. *J. Biomech.* **32**, 11–19.

STETTLER, J. C. & HUSSAIN, K. M. F. 1986 On transition of the pulsatile flow. *J. Fluid Mech.* **170**, 169–197.

STROUD, J. S., BERGER, S. A. & SALONER, D. 2002 Numerical analysis of flow through a severely stenotic carotid artery bifurcation. *J. Biomech. Engng* **124**, 9–20.

VARGHESE, S. S & FRANKEL, S. H. 2003 Numerical modeling of pulsatile turbulent flow in stenotic vessels. *J. Biomech. Engng* **125**, 335–460.

WALLACE, J. M., ECKELMANN, H. & BRODKEY, R. S. 1972 The wall region in turbulent shear flow. *J. Fluid Mech.* **54**, 39–48.

ZHAO, W., FRANKEL, S. H., & MONGEAU, L. G. 2000 Effects of trailing jet instability on vortex ring formation. *Phys. Fluids* **12**, 589–596.